

<https://doi.org/10.1038/s43246-025-00814-2>

Narrowing band gap chemically and physically: conductive dense hydrocarbon

Check for updates

Takeshi Nakagawa¹✉, Caoshun Zhang¹, Kejun Bu¹, Philip Dalladay-Simpson¹, Martina Vrankić², Sarah Bolton³, Dominique Laniel³, Dong Wang¹, Akun Liang³, Hirofumi Ishii⁴, Nozomu Hiraoka⁴, Gaston Garbarino⁵, Angelika D. Rosa⁵, Qingyang Hu¹, Xujie Lü¹, Ho-kwang Mao^{1,6} & Yang Ding¹✉

Enhancing intermolecular interactions can reduce the band gap energy of organic molecules. Consequently, certain polycyclic aromatic hydrocarbons – typically wide-band-gap insulators – may undergo insulator-to-metal transitions under simple compression. This pressure-induced electronic transition could enable the transformation of non-metallic organic materials into states exhibiting intriguing electronic properties, including high-temperature superconductivity. Here we investigate a pressure-induced transition in dicoronylene (C₄₈H₂₀), an insulator at ambient conditions, to a semiconducting state with a resistivity drop of three-orders-of-magnitude at 23.0 GPa. Through the complementary integration of transport property measurements with in situ UV-Visible absorption, Raman spectroscopy and synchrotron X-ray diffraction experiments, as well as first-principles studies, we propose a possible mechanism for the pressure-driven electronic structure evolution of C₄₈H₂₀. The discovery of an intriguing electronic transition at pressures well below the megabar observed marks a promising step towards realizing a single-component purely hydrocarbon molecular metal.

Insulator-to-metal (I-M) transition has been a topic of fundamental interest ever since the introduction of a model for the electronic band structure of solids¹. Back in 1968, Ashcroft pointed out that metallic hydrogen would be a room temperature (RT) superconductor², and since then the realization of metallic hydrogen has been a long-standing challenge in condensed matter physics. However, the experimental confirmation of metallic hydrogen is extremely challenging, requiring ultra-high pressures of at least 350 GPa³. With the rapid advancement of experimental high-pressure techniques, some researchers have claimed the existence of metallic and semi-metallic hydrogen^{4–7}, but an unambiguous experimental confirmation of such observations remains extremely difficult. More recently, efforts have focused on hydrogen-dominant alloys such as binary and ternary metal hydrides, as well as superhydrides, in which the electron density at the hydrogen atoms is pre-compressed, comparable to pure hydrogen compressed to megabar pressure^{8–11}. The hydrogen atoms in these compounds are predicted to have characteristics similar to idealized pure metallic hydrogen at substantially lower pressures.

Along the same lines, organic molecular compounds based on light elements like carbon hold significant potential for achieving high critical temperatures (T_c) superconductivity. Theoretically, carbon- and hydrogen-rich materials are promising candidates, as they can provide the high-frequency phonon modes and strong electron-phonon coupling necessary for such phenomena. This has spurred considerable research into polycyclic aromatic hydrocarbons (PAHs), molecular systems with robust electron-phonon interactions, as a compelling platform for designing high T_c superconductors^{12–14}. Over recent years, many investigations were done to investigate this family of organic compounds under extreme thermodynamic conditions to search for new polymorphs and to understand the mechanism that regulate the creation, stability, and changes of crystal structures of these organic molecules^{15–17}. Reviewing the experimental data so far, studies involving conjugated organic molecules such as PAH solids above 10 GPa are scarce. In general, this is largely down to the widespread misconception that organic crystals are easily decomposed when compressed and the technical difficulties of conducting tests on such delicate

¹Center for High Pressure Science and Technology Advanced Research, 10 Xibeiwang East Road, Haidian District, Beijing, 100094, P. R. China. ²Division of Materials Physics, Ruđer Bošković Institute, Bijenička 54, 10000 Zagreb, Croatia. ³Centre for Science at Extreme Conditions and School of Physics and Astronomy, University of Edinburgh, EH9 3FD Edinburgh, United Kingdom. ⁴National Synchrotron Radiation Research Center (NSRRC), Hsinchu, 30076, Taiwan ROC.

⁵European Synchrotron Radiation Facility (ESRF), 71 avenue des Martyrs, 38000 Grenoble, France. ⁶Shanghai Key Laboratory of Material Frontiers Research in Extreme Environments (MFEE), Shanghai Advanced Research in Physical Sciences (SHARPS), Shanghai, 201203, P. R. China.

✉ e-mail: takeshi.nakagawa@hpstar.ac.cn; yang.ding@hpstar.ac.cn

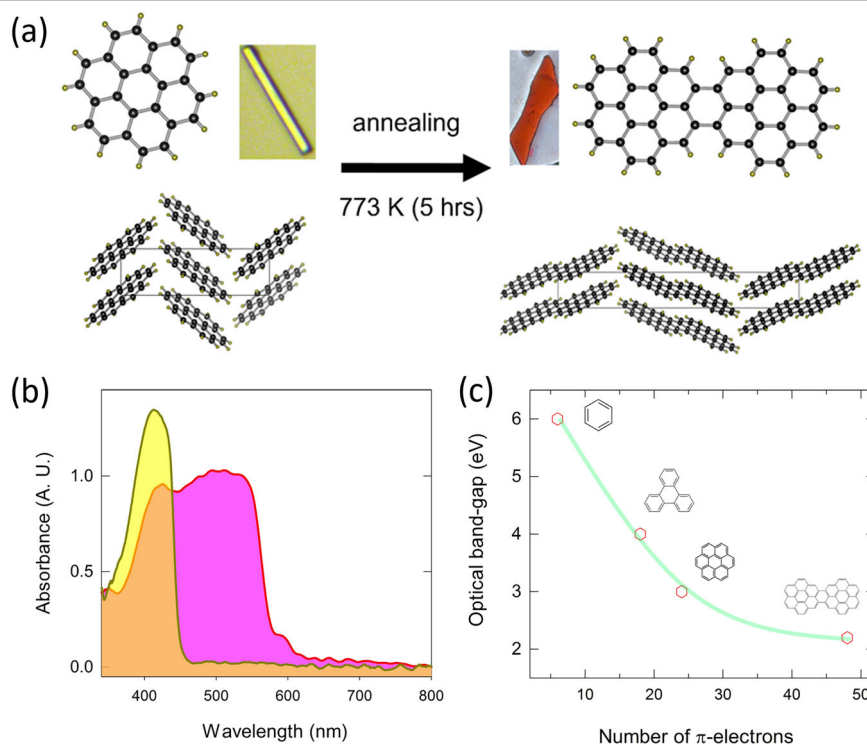
materials. Consequently, the PAH molecules have long been supposed to have minimal structural flexibility under pressure and have been studied using single-crystal measurements only up to 2.1 GPa. Some exceptional examples involve the investigation of the crystal structures of anthracene ($C_{14}H_{10}$) (up to 27.8 GPa)¹⁵, benzo[a]pyrene ($C_{20}H_{12}$) (up to 28.0 GPa)¹⁸, dicoronylene ($C_{48}H_{20}$) (up to 20.2)¹⁹, chrysene ($C_{18}H_{12}$) (up to 20 GPa)¹⁶ and pyrene ($C_{16}H_{10}$) (up to 35 GPa)²⁰. Contrary to the previous belief that large organic molecules have low conformational flexibility under pressure, Zhou et al. demonstrated that gradual compression results in continuous compaction of molecular packing, eventually leading to previously unknown molecule curvature²⁰. Yet, the above studies primarily address the mechanical response of PAH crystallographic network from a structural perspective, enhancing our understanding of their structural dynamics and stability under high pressure. There have been many efforts, but it is still not easy to bridge the complex structure-property gap of PAHs at high pressures.

Another, rather recent, Aschroff's theoretical study highlighted that there may exist a narrow pressure range between 180–200 GPa where benzene (C_6H_6) display molecular metallic states. The concept involves the synthesis of hydrogen and carbon “alloy” that can effectively decrease its band gap at RT and by applying high-pressures to enhance electron-phonon interaction that can potentially induce transition into a metallic state²¹. Similarly, theoretical calculations on triphenylene ($C_{18}H_{12}$) revealed that it may turn metallic at 180 GPa²². The magnitude of their electron-phonon interaction depends on the distance between the nearest-neighbour (nn) molecules²³ and thus, the knowledge of the intermolecular distance can be critical in understanding the mechanism for physical properties under high pressure. Despite several experimental attempts to discover a metallic molecular state in a carbon-hydrogen system, the only PAH molecule that has been reported to have electronic transition is pentacene ($C_{22}H_{14}$), where semiconductor to metallic transition was observed at 27 GPa by Drickamer in 1962²⁴. However, this phenomenon has not been reproduced, as other studies found pentacene remain semiconducting up to 11 GPa, loses their molecular form beyond this pressure^{25–27}. Other attempts to discover a metallic state in PAHs have only confirmed the occurrence of an irreversible chemical process at 8–20 GPa^{28–30}, which is far below the expected critical pressure for the formation of a metallic state.

To achieve a conductive state in PAHs, the band gap energy must be further pre-compressed at ambient conditions and improve the chemical stability of the molecule so that the band gap can be closed by physical compression before the molecule decomposes. It is well-known that increasing the number of aromatic rings, or more specifically, the amount of π -electrons, allows for effective tuning of the band gap energy of PAH molecules³¹. As an illustration, C_6H_6 has an optical band gap of about 6 eV with 6 π -electrons³², $C_{18}H_{12}$ has an optical band gap of 4 eV with 18 π -electrons³¹, and $C_{24}H_{12}$, which has 24 π -electrons, has an optical band gap of 2.8 eV (Scheme 1c)³³. This is due to the condensation of strongly conjugated π -systems. In addition, our most recent high-pressure investigations on large PAH molecules, i.e., $C_{24}H_{12}$ where the C_6H_6 rings are fused together in a disc-like fashion, have shown that they can maintain their chemical stability up to pressures exceeding 20 GPa³³. These signatures in a compressional behavior of $C_{24}H_{12}$ are revealing indication that large PAH molecules show a potential for high-pressure superconductivity and the I-M transition.

Herein, we focus on the effects of pressure on the large PAH molecule, $C_{48}H_{20}$, which is formed by chemical fusion of two $C_{24}H_{12}$ molecules, resulting in an optically red single crystal. The workflow utilizes various techniques under mechanical compression-responsive conditions, including optical absorption measurements, electrical resistance measurements, Raman and IR spectroscopy data collection, synchrotron single crystal X-ray diffraction (SC-XRD) and powder X-ray diffraction (SP-XRD) experiments, and ab initio calculations to support the experimental data. At ambient conditions, the band gap energy of $C_{48}H_{20}$ is reduced to 2.21 eV from 2.8 eV for the $C_{24}H_{12}$ monomer. We observed a continuous closing of the band gap of $C_{48}H_{20}$ from 2.21 eV at ambient conditions down to 0.7 eV at 33.6 GPa, accompanied by a change in the optical color of the crystal from red to completely black. Our findings, corroborated by electrical resistance studies that varied with temperature, show that the semi-metallic character of $C_{48}H_{20}$ becomes apparent in the pressure range of 23.0–38.0 GPa. In addition, the compressional behavior of $C_{48}H_{20}$ is shown by pressure-driven XRD experiments and complementary Raman spectroscopy measurements, which make use of soft structural distortions to allow for delicate manipulation of its band gap. In particular, the SC-XRD revealed that the semi-metallic state occurs when the intermolecular n C-C distance is shorter

Scheme 1 | a Dicoronylene ($C_{48}H_{20}$) obtained via vapor phase fusion reaction of coronene ($C_{24}H_{12}$) molecules. Molecular structures, crystal structures and optical micrographs of $C_{24}H_{12}$ and $C_{48}H_{20}$. b Absorption spectra (Absorbance Unit, A.U.) of $C_{24}H_{12}$ (yellow) and $C_{48}H_{20}$ (pink). c Optical band gaps derived from absorption spectrum for four PAH molecules plotted against the number of π -electrons. Green line is for the guide to the eyes.



than 2.8 Å and the irreversible chemical reaction takes place at a C-C distance of 2.6 Å. As far as we know, no other single-crystal data on PAHs have been reported to date that provide meaningful information for interpreting predictions and understanding the relationships between their structure and properties. The first-principles calculations provide information about the chemical bonds and electronic properties and confirm the experimental results, according to which the band gap is closed under physical pressure at 28.0 GPa. We have demonstrated that the increasing number of π -electrons can chemically pre-compress the band gap significantly, whereupon physical compression can further reduce the band gap, leading to a transition from insulator to semiconductor in $C_{48}H_{20}$. This is a huge advantage over ordinary so-called superhydride materials, which require high-pressure and high-temperature synthesis in the diamond anvil cell (DAC), resulting in multicomponent, multiphase crystals on a micrometer scale^{34,35}. The finding of an electronic transition at a pressure that is far lower than one megabar is a piece of hopeful news for the potential creation of a wholly organic molecular single-component metal in large PAH molecular crystals system.

Results and discussion

Characterization at ambient pressure

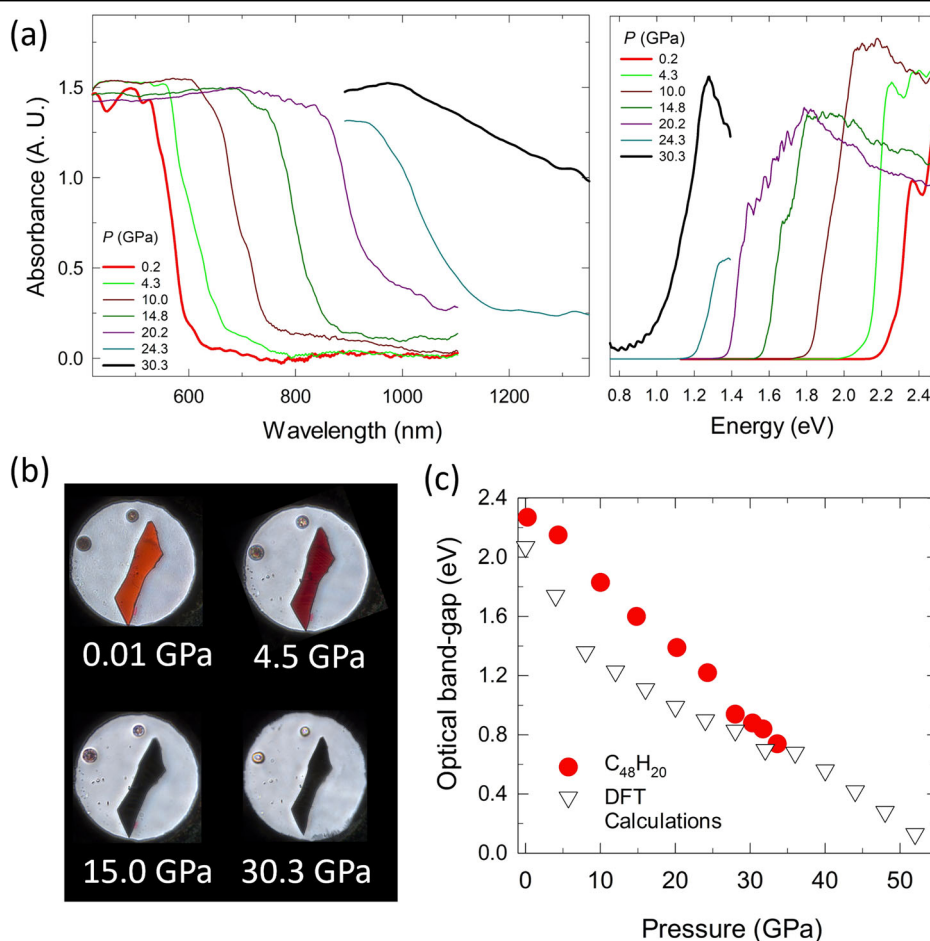
Details about the preparation of $C_{48}H_{20}$ can be found in our previous publication¹⁹. The SC-XRD of $C_{48}H_{20}$ under ambient conditions shows that it crystallizes in a monoclinic β -herringbone assembly with the centrosymmetric space group $P2_1/c$, whose structure matched those of Goddard et al.³⁶. Drawing the comparison, the structure refinement against SC-XRD data at ambient conditions yielded the following lattice metrics of $C_{48}H_{20}$: $a = 10.3940(8)$ Å, $b = 3.8402(3)$ Å, $c = 31.990(3)$ Å, $\beta = 90.248(2)^\circ$, $V = 1276.89(17)$ Å³, with the final anisotropic full-matrix refinement converging at $R_1 = 2.4\%$ for the observed data and $wR_2 = 7.4\%$ for all data. Details of the crystal structure extracted from the refined SC-XRD data can

be found in the Supplementary information Table S1. The crystalline $C_{48}H_{20}$ exhibits strong red fluorescence emission bands when irradiated with lasers emitting in visible frequencies. The very strong fluorescence obscures the weak Raman modes recorded with laser sources at wavelengths of 633 and 532 nm. Out of the 204 active Raman modes of $C_{48}H_{20}$, only 20 lines were observed when the laser excitation wavelength was 1064 nm (Supplementary Fig. 1). To estimate the optical band gap of $C_{48}H_{20}$ at ambient conditions, the absorption spectrum was first transformed spectrum into Tauc plot, $\alpha^{1/2}$ vs $h\nu$ curve, where α is the absorption coefficient, h is Planck constant, and ν is the frequency of the photon. The region showing a steep, linear increase of light absorption with increasing energy is characteristic of semiconductor materials, and the x-axis intersection point of the linear fit gives an estimate of the band gap energy^{37,38}. This value is much smaller than that of other PAHs, such as, C_6H_6 (6.0 eV), naphthalene ($C_{10}H_8$) (4.2 eV), phenanthrene ($C_{14}H_{10}$) (4.16 eV), $C_{18}H_{12}$ (3.95 eV), tetracene ($C_{18}H_{12}$) (2.54 eV), pyrene ($C_{16}H_{10}$) (3.03 eV), and $C_{24}H_{12}$ (2.8 eV)^{31–33,39,40}. The pressure-dependent electronic structures at various pressure points were calculated using density functional theory (DFT) based on the ambient pressure structure to predict the pressure required for the band gap closure. The band gap closure for $C_{48}H_{20}$ was expected to occur at roughly 50.0 GPa, which is still quite high for organic molecules, but certainly achievable, especially when compared to predictions for other PAH molecules, such as 190 GPa for C_6H_6 , 160 GPa for $C_{18}H_{12}$, and 117 GPa for benza[a]anthracene ($C_{18}H_{12}$)^{14,22,41}.

Optical absorption spectroscopy and band gap closure

Turning our attention to the physical properties, the in-situ UV-vis absorption spectra upon compression are shown in Fig. 1. Upon compression, the absorption increases and broadens, corresponding to the change in the optical color of the crystal from red to dark red, opaque black

Fig. 1 | In-situ pressure-dependent absorption spectra of a single crystal $C_{48}H_{20}$. **a** Optical absorption spectra recorded during compression from ambient pressure up to 30.3 GPa, and their corresponding Tauc plot to estimate the optical band gap energies. **b** Optical images of $C_{48}H_{20}$ at each pressure point where the color of the crystal changes from red, dark-red, opaque black and black. **c** Estimated and calculated band gap energies as a function of pressure.



above 10.0 GPa, and completely black above 24.0 GPa (Fig. 1b). The transformation of this crystal color is reversible, with the original crystal color being restored when the applied pressure of 14.0 GPa is completely released (Supplementary Fig. 2a), but irreversible when it is released from 60.0 GPa (Supplementary Fig. 2b). At higher pressures, a broadening and continuous red-shift of the UV-Vis absorption spectra extends to longer wavelengths and eventually covers the entire visible and near-infrared (NIR) range. Above 24.0 GPa, the absorption edge shows a discontinuous, sharp red-shift, indicating a structural transition accompanied by a complete blackening of the crystal, where it absorbs all visible and NIR light, i.e., 0% transmittance. Figure 1c shows the optical band gap as a function of pressure. The optical band gap of $C_{48}H_{20}$ extracted from the absorption spectra exhibits systematical decrease from 2.2 eV at ambient conditions to 1.2 eV at 24.0 GPa, and a discontinuous drop to 0.9 eV at 30.3 GPa. When the applied pressure was further increased above 30.0 GPa, the spectra continued to show a red-shift, but it was not possible to accurately estimate the optical band gap because they were outside the measurable limit. At this point, we observed that the crystal reflects the light shed from the top, which might be an indication of a transition from the insulator to semi-metallic state (Supplementary Fig. 2). Figure 1c also shows the pressure evolution of the band gap derived by DFT calculations. Although, the optical band gap does not perfectly match the electronic band gap and DFT calculations often underestimate the band gap energies, they can provide an accurate approximation. Indeed, the calculated values agree well with the extrapolation of the extracted optical band gap energies from this experiment.

Above 40.0 GPa, the pressure-dependent absorption edge changes abruptly, returning to a shorter wavelength (Supplementary Fig. 3). The blue shifts of the absorption edge are ascribed to the reopening of the band gap, which is accompanied by a change in the optical color of the crystal from black to brown and the disappearance of the reflected light. The reopening of the band gap continues up to 60.0 GPa, with an estimated optical band gap of 2.53 eV, which is larger than at ambient conditions (Supplementary Fig. 4). The optical color of the crystal and the band gap energy remain the same during the pressure release down to 13.0 GPa; when the pressure is completely released, the color of the crystal changes into opaque black with the estimated band gap energy of 1.72 eV. The optical discoloration of the crystal to brown and the reopening of the band gap are clear signs of the loss of conductivity and the possible transformation into a new insulating state.

The insulator to semiconductor transition

The effects of pressure on the electronic properties and possible pressure-induced electronic transitions of $C_{48}H_{20}$ were further investigated by electrical transport measurements. At ambient conditions, $C_{48}H_{20}$ is an electrical insulator with the resistivity value beyond the sensitivity of the equipment used. With increasing pressure in a DAC at RT, we observe a pronounced decrease in its electrical resistance (Fig. 2). The resistance was

calculated according to the Van de Pauw method using the equation:

$$\exp(-\pi R_1/R_s) + \exp(-\pi R_2/R_s) = 1 \quad (1)$$

where R_1 and R_2 are the two resistances measured by the four-probe method and R_s is the sheet resistance⁴². The electrical resistivity ρ was calculated as $\rho = R_s \times t$, where t is the thickness of the crystal (approximately 10 μm for the typical $C_{48}H_{20}$ crystal). Up to a pressure of about 15.0 GPa, the resistivity steadily decreases from ambient pressure as pressure increases. Above 15.0 GPa, the rate of resistance drop accelerates, with the resistivity value dropping by three orders of magnitude up to around 30.0 GPa. During compression, the optical color of the crystal was observed to change from red to black at 25.0 GPa. Above ~ 25 GPa, $C_{48}H_{20}$ undergoes a pressure-induced insulator-semiconductor transition, as evidenced by a decrease in resistance and a change in the color of the crystal. To confirm the transition, the temperature dependent resistance measurements were done at three pressure points, i.e., 13.0, 23.0 and 38.0 GPa, as shown in Fig. 2b. The electrical resistance at 13.0 GPa instantly increases with decreasing temperature, which is a typical insulator character. The electrical resistance at 23.0 GPa, on the other hand, increases exponentially with decreasing temperature, which is a typical semiconducting character, confirming the insulator-semiconductor transition. A rapid increase in the RT resistance value was observed above 40.0 GPa (Supplementary Fig. 5), which corresponds to pressure-induced amorphization and agrees with band gap opening observed in UV-Vis absorption measurements under high pressure.

Evolution of crystal lattice vibrational modes at high pressure

To investigate the effects of compression on intermolecular interactions, we conducted an in-situ high-pressure Raman spectroscopy experiment at RT up to 49.0 GPa. While spectroscopic data do not yield direct insights into the structure of solid materials, it is noteworthy that our group recently conducted a study on the vibrational spectroscopy of $C_{48}H_{20}$ at pressures up to approximately 20 GPa. This study revealed enhanced intermolecular interactions, which are responsible for alterations in crystal color and diminished PL emission, as hidden Raman modes were detected using a 532 nm green laser above 4.5 GPa¹⁹. In essence, the assignment of Raman bands can reveal subtle energy differences between the vibrational modes of the external and internal crystal lattice, which are influenced by molecular interactions. Since the outer vibrational modes in the low-frequency region of the Raman spectrum are particularly sensitive to the crystal shape and molecular arrangements within the unit cell, the Raman tool complements the XRD expertise by visualizing details of possible structural changes. Within this interpretation, the Raman spectra were obtained with a laser excitation at 532 nm with a normal power density of 0.5 $\text{mW}/\mu\text{m}^2$ to avoid spectral changes due to radiation damage. At ambient pressure and below 3.0 GPa, all Raman modes are obscured by the strong fluorescence of the

Fig. 2 | Electrical transport properties of $C_{48}H_{20}$ under pressure. a RT resistivity of $C_{48}H_{20}$ at various pressure points. **b** Temperature-dependent resistivity of $C_{48}H_{20}$ measured during heating from 200 K to 290 K with a van der Pauw setup at 13.0, 23.0 and 38.0 GPa.

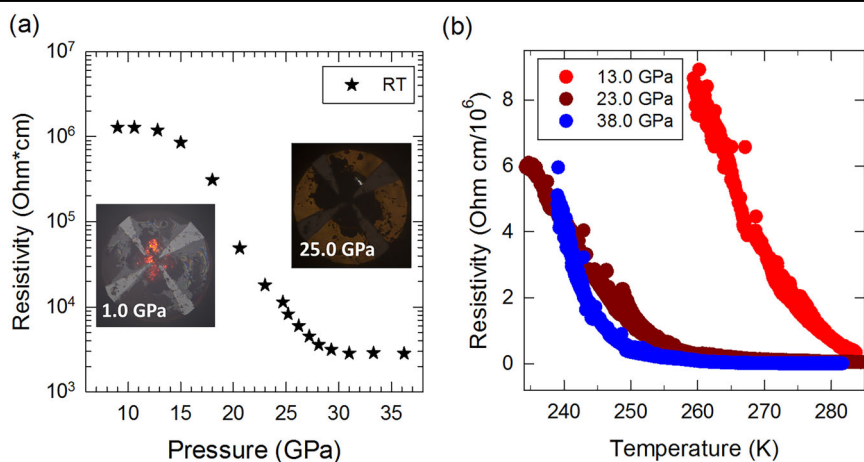
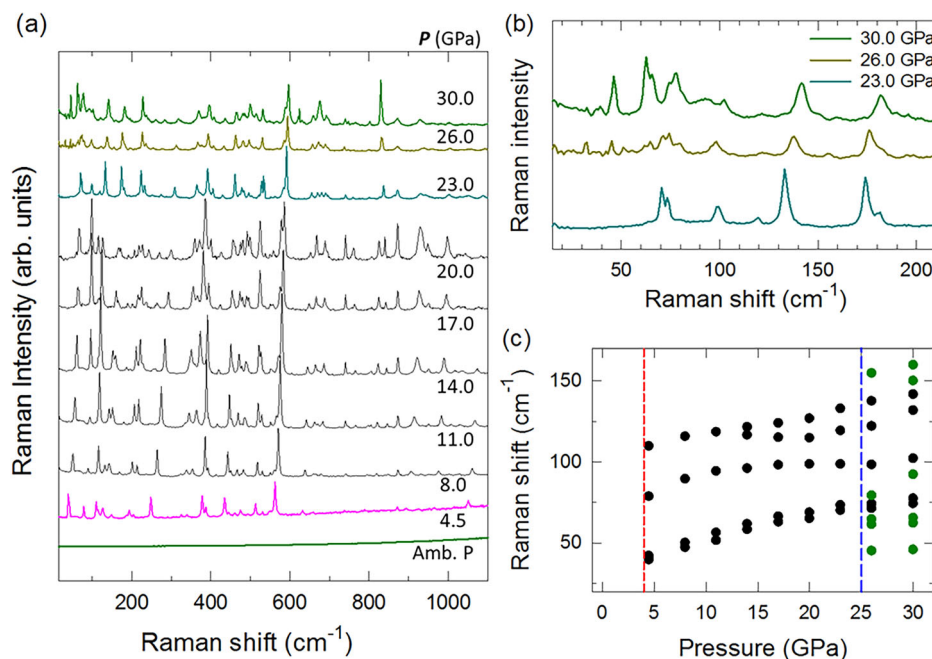


Fig. 3 | High-pressure Raman spectroscopy measurements. **a** Pressure-dependent Raman spectra of a single-crystal of $C_{48}H_{20}$ recorded during compression using a 532 nm excitation laser. **b** Selected Raman spectra in the low-frequency region of $C_{48}H_{20}$ at pressures above 20.0 GPa. New Raman modes appeared above 23.0 GPa, indicating structural transition to new polymorph. **c** Pressure-dependence of Raman shifts. Raman modes were not observed between ambient pressure and 4.0 GPa owing to fluorescence (as illustrated by the red dotted line). The phase transition was observed at pressures above 23.0 GPa (blue dotted line).



sample, consistent with earlier study¹⁹. Fig. 3 shows the evolution of the Raman modes in $C_{48}H_{20}$. The intensity of the entire Raman modes decreases at 23.0 GPa, which coincides with the change in the color of crystal to complete black. Looking below 200 cm^{-1} , significant changes in the intermolecular modes take place at 26.0 GPa, with the two lattice modes at 70.0 cm^{-1} and 74.3 cm^{-1} splitting into two doublets. Also, the emergence of new low-frequency mode at 45 cm^{-1} provides additional evidence that structural shifts towards lower symmetry might be feasible (see Fig. 3b, c). The low-energy lattice modes in particular are sensitive to changes in crystal structure, and any change in this region can be directly associated with local structural changes, leading to phase transitions⁴³. Namely, despite the absence of alterations in crystal symmetry at 26.0 GPa as detailed in Ref. 19, the progression of the unit cell volume beyond 15.0 GPa, may suggest a potential phase transition at this pressure point. Finally, at 40 GPa, all Raman modes disappear, indicating the occurrence of crystal amorphization transformations or eventual irreversible chemical reaction beyond this pressure.

When pressure was released from 43 GPa, both lattice and internal modes reappeared below 30 GPa. The fluorescence emission was also recovered below 10 GPa, and all the Raman modes are obscured by strong fluorescence intensity. This indicates that the loss of Raman modes at 40 GPa is indicating the occurrence of crystal amorphization transformation. When the pressure was released from 49 GPa, the fluorescence emission was not recovered even when the pressure was completely released. We observed the recovery of very weak lattice modes and strong internal modes. Such irreversible spectral changes are indicative of permanent structural modifications, such as occurrence of polymerization. (Supplementary Figs. 6 and 7)

To investigate further the effects of pressure on $C_{48}H_{20}$ and their reversibility, we carried out IR measurements up to a maximum pressure of 39.0 GPa and decompressed to ambient conditions. (Supplementary Fig. 8) After decompression from 39.0 GPa, an almost complete recovery of the original spectral features was observed at 0.2 GPa, which also supports that the $C_{48}H_{20}$ maintains its molecular form during phase transition above 23.0 GPa. Compared to other compounds, C_6H_6 starts to produce amorphous hydrogenated carbon or carbon nanotubes at pressures higher than 16.2 GPa, according to published IR spectroscopy observations^{44,45}.

Structural evolution under high pressure at RT

To gain intricate understanding of the interplay between the structure and property under high pressure and to address the structural stability of

$C_{48}H_{20}$, we carried out an in-situ high pressure SP-XRD and SC-XRD experiments reaching pressures of up to 60.0 GPa and 26.2 GPa, respectively. Figure 4a depicts selected SP-XRD profiles of polycrystalline $C_{48}H_{20}$ obtained at various pressure points. At 0.3 GPa, the Le Bail fit of the SP-XRD data shows that the reflection intensities roughly correlate to the single-crystal data obtained at ambient pressure (Fig. 4b, top). Although there are alternations in intensity ratios the (100) and (102) Bragg reflections, structure transition occurs at pressures beyond 18.7 GPa. This transformation is observed by the splitting of the diffraction peak at $4^\circ 2\theta$, which suggests that a reduction in symmetry has taken place (Fig. 4a–c). Under ambient conditions, $C_{48}H_{20}$ has a monoclinic β -herringbone structure (Fig. 4d, left panel) with space group $P2_1/c$, which encompasses two translationally inequivalent molecules per unit cell centered on positions 0,0,0 and $\frac{1}{2}, \frac{1}{2}, 0$. The $C_{48}H_{20}$ molecules, in particular, are arranged in layers parallel to the bc plane, with the long molecular axis roughly perpendicular to the plane of the layer, whilst neighboring molecules within a layer are twisted with respect to each other, forming a distinctive herringbone stacking. Figure 4d, left panel depicts the projection of $C_{48}H_{20}$ onto the bc plane, showcasing two such layers and the arrangement of the molecules inside those layers. Our best attempts to index the resulting diffraction data yield a unit cell having the centrosymmetric triclinic symmetry with space group $P-1$ (Fig. 4a, b, bottom). The reduction of symmetry from monoclinic to triclinic is consistent with symmetry breaking and group-subgroup relations (Fig. 4e). The peak position extraction from an indexed powder diffractogram was used to evaluate the unit cell metrics of polycrystalline data at all pressure points. Supplementary file contains a summary of $C_{48}H_{20}$ unit cell metrics acquired from the Le Bail refinement against SPXRD data ($\lambda = 0.6199 \text{ \AA}$) at RT (see Supplementary Table S2). Despite the change in symmetry, the arrangement of the molecules within the unit cell for these two phases is likely to be quite similar. The correlations between the cell parameters used in the literature^{46,47} and the characteristic distances (h , x , and y) are shown in Fig. 4c, right panel. The phase transition at 23.0 GPa agrees well with the insulator-semiconductor transition observed in UV-Vis absorption, electrical transport, and Raman measurements.

At pressures higher than 38.0 GPa, the combination of the size and strain-induced effects led to a noticeable additional broadening of the observed XRD peaks, gradual fading of the triclinic (001) and (011) Bragg peaks and the appearance of amorphous-like broad peaks. When the pressure exceeded 62.0 GPa, the diffraction peaks from the sample become barely distinguishable from the background noise. However, when the

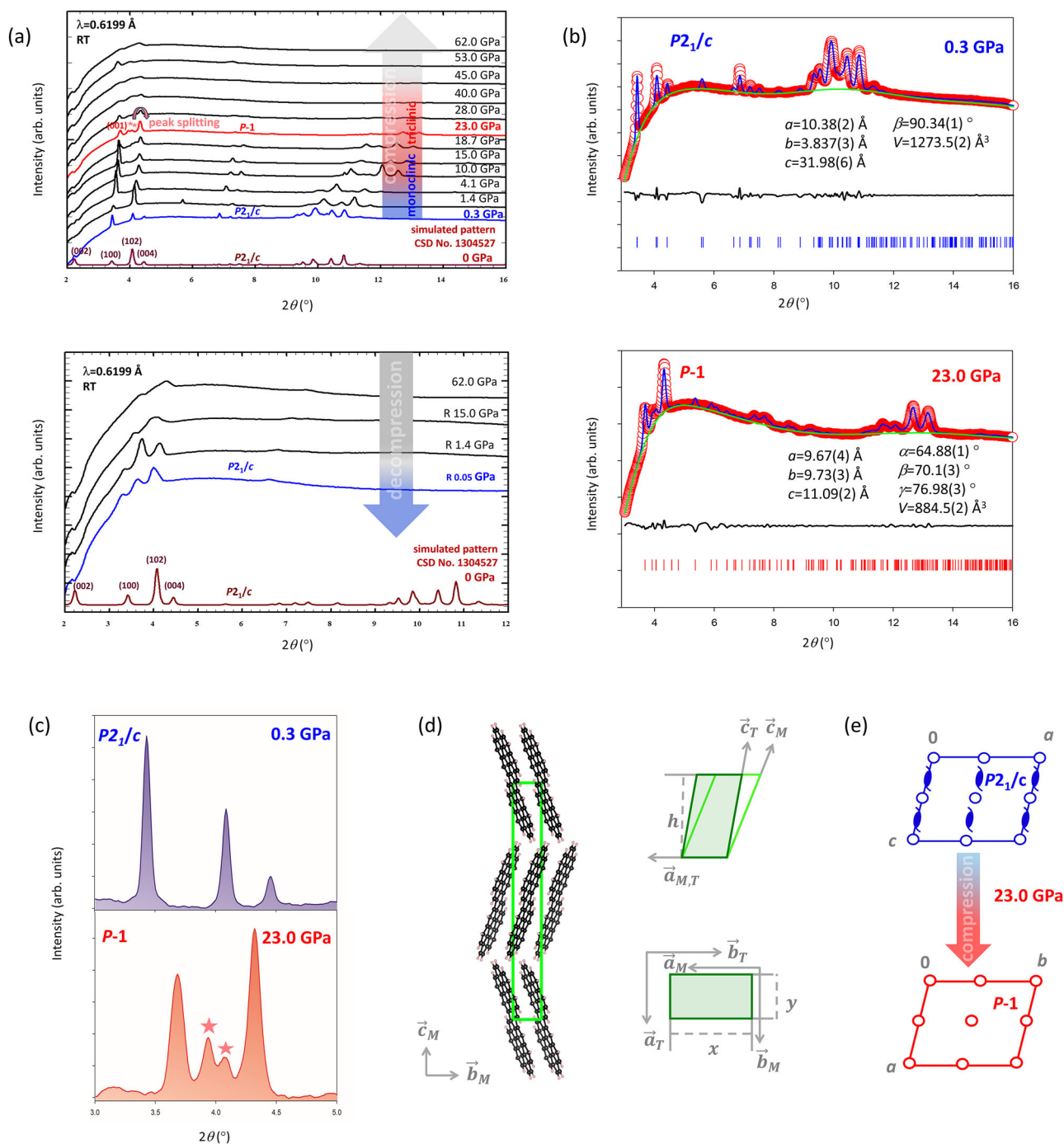


Fig. 4 | High-Pressure SPXRD measurements and structure analysis of $C_{48}H_{20}$.

a Selected in-situ high-pressure SPXRD profiles upon compression (top) and decompression (bottom). The experimental data at 0.3 GPa match the simulated SPXRD pattern of $C_{48}H_{20}$ collected at ambient conditions (CSD No. 1304527)³⁶. **b** (a) Observed (red circles) and calculated (solid blue line) SPXRD profiles obtained from the Le Bail fit against the PXRD data of $C_{48}H_{20}$ at 0.3 GPa (top) and 23.0 GPa (bottom). The lower solid black line depicts the difference profiles. The solid blue and red vertical tick marks show the reflection positions of the monoclinic and triclinic $C_{48}H_{20}$ phases, respectively. The lower solid green lines indicate the fitted background contribution. **c** Zoomed-in look at the XRD patterns at the critical

pressure points in comparative style serving as a signature of a crystal structure alteration. For clarity, background subtraction was applied. **d** Crystal packing of $C_{48}H_{20}$ at ambient conditions, viewed along a axis (left panel). Cell conventions for oligoacenes as used in literature⁴⁷ (right panel). The index M stands for monoclinic cell, and T for triclinic cell. The characteristic distances are the layer thickness, h , and the long and short herringbone lengths x and y . **e** Schematic projection of the equatorial plane of point groups $2/m$ in the monoclinic phase and -1 in the triclinic phase during the structural transition triggered by hydrostatic pressure, in accordance with symmetry breaking and group-sub group relations.

pressure is released to ambient conditions, the initial monoclinic phase partially recovers, as do the (002), (100), (102), and (004) reflections. Yet, the lower intensities and larger peak widths of decompressed monoclinic Bragg reflections indicate a high amount of topological disorder in the relaxed sample.

To obtain more comprehensive data on the molecular structure and evolution of periodic arrangement in three-dimensional space of $C_{48}H_{20}$, we collected SC-XRD data at pressures of 3.3, 10.3, 19.2, 26.2 GPa. The refined unit cell parameters from these measurements are listed in Table 1, where the structures were solved as monoclinic crystals in space group $P2_1/c$. The

Table 1 | Summary of C₄₈H₂₀ unit cell metrics and reliability factors obtained from the structure refinement of the SC-XRD data

P (GPa)	a (Å)	b (Å)	c (Å)	β (°)	V (Å ³)	nn C-C dist.(Å)	nn H-H dist.(Å)	s.g.	R _{wp}
0.0 ^a	10.3940(8)	3.8402(8)	31.990(3)	90.248(2)	1276.89(17)	3.474(3)	2.354(1)	P2 ₁ /c	7.4
3.3	9.887(7)	3.4964(2)	30.951(2)	90.18(2)	1070.0(8)	3.191(6)	2.14(2)	P2 ₁ /c	1.62
10.4	9.743(4)	3.2674(1)	30.563(1)	90.314(10)	972.9(2)	2.913(4)	2.07(3)	P2 ₁ /c	1.31
19.2	9.515(6)	3.1218(2)	30.0280(16)	90.462(16)	891.9(6)	2.801(4)	1.91(4)	P2 ₁ /c	1.91
26.2	9.466(13)	3.0474(3)	29.701(4)	90.36(4)	856.7(12)	2.724(7)	1.87(7)	P2 ₁ /c	1.81

^aResulting structural parameters and reliability indices of C₄₈H₂₀ against SC-XRD data collected at ambient conditions (λ = 0.7103 Å).

crystallographic information on the complete structure solution and refinement are listed in Tables S4–S7. An anisotropic response to compression along three crystallographic axes was also found, with the lattice parameter *b* decreasing by 12.8% at 26.2 GPa, while *a* and *c* were reduced by 4.2% and 4.0%, respectively, resulting in a total volume reduction of 20.0%. The intermolecular distances were also calculated on the basis of the experimental data. At ambient pressure, the C–C and H–H distances between the atoms of the nn molecules were 3.474(3) Å and 2.354(1) Å, respectively. At 26.2 GPa, analysis of the SC-XRD data shows that the same intermolecular C–C and H–H distances were reduced to 2.724(7) Å and 1.87(7) Å, respectively. The structural models, the pressure–volume data points and the lattice parameters obtained from SC-XRD and DFT calculations showed good agreement with each other. Compressing the crystals from 19.2 to 26.2 GPa drastically altered their appearance. The data collected promptly following the pressure increase to 26.2 GPa yielded a good structural model that agrees with the data obtained at lower pressures. Subsequent data acquired on the identical crystal at the same pressure approximately 40 minutes later indicated a significant degradation in crystal quality (Supplementary Fig. 9), as most of the reflections associated with the crystal had almost disappeared, while the remaining reflections appeared streaky and had a very weak intensity. This indicates a gradual structural phase shift at this pressure, in agreement with the transformation observed by SP-XRD between 18.7 and 23.0 GPa.

These fingerprints are consistent with the critical intermolecular distances proposed by previous molecular-dynamics simulations of C₆H₆ at 23.0 GPa and 540 K. According to them, intermolecular chemical bonding can only take place at an intermolecular distance of 2.7 Å, and the threshold for irreversible reactions starts when the distance between the nn C–C bonds is close to 2.5–2.6 Å²⁹.

First-principles investigation on high-pressure structural evolution

With the fair compressional behavior of C₄₈H₂₀ in hand, we explored the band gap of C₄₈H₂₀ in further depth. Figure 5 depicts the evolution of the volume of the unit cell, the electron localization function (ELF), and the band structures of C₄₈H₂₀ molecules. The pressure–volume data points obtained from SP-XRD, SC-XRD and DFT calculations are almost identical, while the structure in space group *P*2₁/*c* remains monoclinic (Fig. 5a). A third-order Birch–Murnaghan equation of state was used in the EoSFIT software⁴⁸ to fit the pressure–volume datapoints for SP-XRD (*V*₀ = 1241.4(2) Å³, *K*₀ = 9.0(3) GPa) and SC-XRD (*V*₀ = 1259.6(2) Å³, *K*₀ = 9.1(2) GPa) data. The ELF calculations based on the structural information at ambient pressure and 26.2 GPa (Fig. 5b) show that the van der Waals space between C₄₈H₂₀ decreases due to the compression of the intermolecular distances and the rotation of the molecules. However, the expected overlap in the intermolecular charge density was not found in these experiments. Calculations of the electronic density of states (eDOS) derived from the resolved crystal structures at different pressure points indicate that the band gap of C₄₈H₂₀ decreases significantly under pressure, ultimately leading to its classification as a poor metal at 28.0 GPa (Fig. 5c). The observed color change of the crystals may be interpreted in terms of this backdrop.

During compression, the C₄₈H₂₀ molecules are rearranged in terms of distances and angles in their herringbone motif, resulting in a gradual

darkening of the optical crystal colors and an enhancement in intermolecular interactions. We have observed that C₄₈H₂₀ undergoes a phase transition at about 23.0 GPa with a slightly altered crystal structure, although the exact pressure probably depends on the hydrostatics of the sample. The underestimation of the band gap and the metallization pressure could be due to the fact that this rearrangement of the molecules was not taken into account. Our optical and structural findings indicate that as the nn C–C distance for C₄₈H₂₀ approaches 2.7 Å under pressure, intermolecular interactions increase and the optical band gap quickly reduces up to 34.0 GPa. The molecular units are stable up to 43 GPa, and the equation of state fitting predicts a C–C distance of 2.6 Å at roughly 40.0 GPa (Supplementary Fig. 10), assuming the compressibility remains constant across different molecular arrangements.

Conclusion

With the aim of exploring superconductivity in a compound consisting of only carbon and hydrogen, we studied the pressure-triggered physical features which manifest in a pictorial structural transition, a tunable band gap evaluation, and altered electric conductive behavior of C₄₈H₂₀, providing evidence for the semi-metallic nature of C₄₈H₂₀. The optical features and the electrical resistance signature indicate transition from insulator to semiconductor in the pressure range between 23.0 and 38.0 GPa. Physical compression reduced the band gap of C₄₈H₂₀ from 2.2 eV at ambient conditions to 0.7 eV at 34.0 GPa, and beyond 23.0 GPa an insulator–semiconductor transition occurred. We discovered the first large PAH to undergo the transition from an insulator to a semiconductor at pressures considerably below megabar. The abrupt phase transition at 23.0 GPa was coupled with a change in crystal color from red to black, a narrowing of the band gap below 1.0 eV at 24 GPa, and an increase in intermolecular interaction. We also demonstrated that the presence of an intermolecular C–C distance less than 2.8 Å results in the semi-metallic state, and that an irreversible chemical reaction occurs at a C–C distance of 2.6 Å, and thus supplemented the bridging of the structure–property landscape in C₄₈H₂₀. In addition, C₄₈H₂₀ shows remarkable chemical stability, with an irreversible chemical reaction occurring at a pressure of 46 GPa. This single-component, single-phase single crystal of pre-compressed large PAH molecules is stable under ambient conditions and may be thoroughly characterized prior to the application of physical compression. The pressure responses of the other large PAH molecules to a possible transition to the metallic and superconducting state should be further investigated in the light of our findings.

Experimental Section

Sample Preparation and Characterization

The single-crystals of C₄₈H₂₀ were obtained by the vapor phase fusion reaction of C₂₄H₁₂ purchased from TCI chemical (> 95%). The details of crystal preparation, characterization under ambient conditions, and addressing the structure-to-optical properties relationship below 20 GPa are discussed in recent paper¹⁹.

High-Pressure Electrical Measurements

The electronic transport properties under high pressure and low temperature were investigated via van der Pauw electrical conductivity method in a

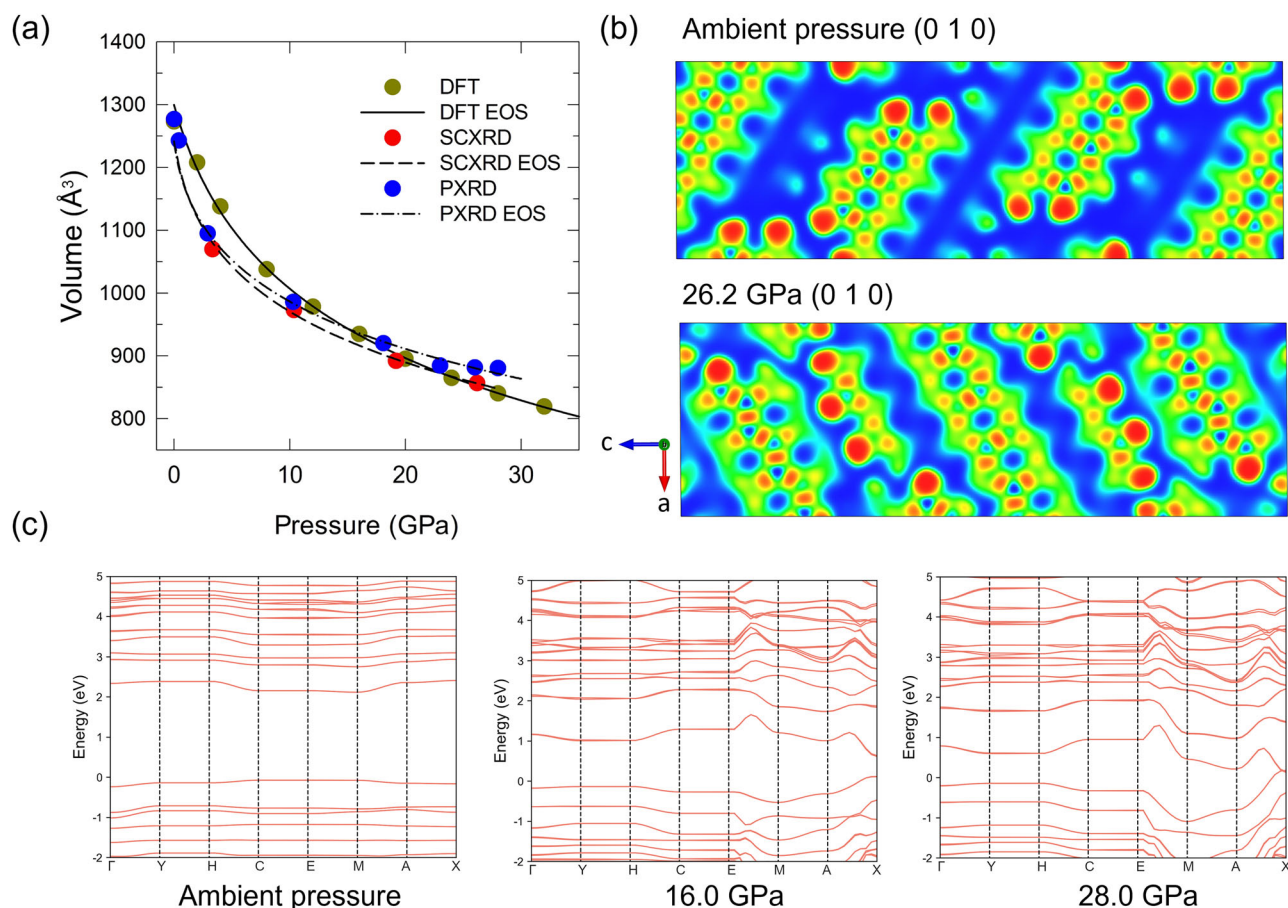


Fig. 5 | Equation of states and electronic structures. **a** The P-V equation of states based on high-pressure experiments and DFT calculations. The solid and dashed lines represent the third-order Birch-Murnaghan equation of state fitted to the volume data. **b** The charge density distribution of C₄₈H₂₀ at ambient pressure and

26.2 GPa calculated from crystal structures obtained from SC-XRD data. **c** Selected band structures at 1 bar, 16.0 and 28.0 GPa. The HOMO and the LUMO come into contact at 28.0 GPa. The distance between the high-symmetry points is normalized for clarity.

symmetric DAC. The pressure was generated by a pair of diamonds with a 300 μm diameter culet. A rhenium gasket was pressed and drilled hole at the center of the gasket with a diameter of the diamond culet. A cubic boron nitride (c-BN)-epoxy insulation layer was prepared to protect the electrode leads from the metal gasket. A hole with a diameter of 150 μm was drilled in the center of the c-BN as a sample chamber to place the C₄₈H₂₀ sample with NaCl as the pressure transmitting medium (PTM). Four platinum strips were arranged so that they touched the sample in the chamber. The first round experiments at different pressure-temperature conditions were performed with a laboratory designed electrical transport system (with optical window) using a Keithley 6221 current source, a 2182 A nanovoltmeter, and a 7001 switching device as current source, voltmeter, and voltage/current switch, respectively. The pressure at the sample chamber was measured using the ruby and diamond fluorescence method. The high-pressure experiment on electrical transport was carried out in the second round using the Quantum Design System for measuring physical properties with 23 mm CuBe cells.

Optical Spectroscopy

The measurements of UV-Vis absorption and optical images were performed with the in-house developed Gora-UVN-FL (Ideaoptics, Shanghai) micro-region spectroscopy system. A single-crystal dicoronylene was loaded together with a ruby ball into the sample chamber of a symmetric Mao-type DAC with 400 μm culet-sized low-fluorescent anvils. Si-oil was used as PTM. Each pressure point was determined by the fitting pressure shift of the ruby fluorescence line. The laser power and acquisition time were carefully adjusted prior to take absorbance at ambient conditions, so that we obtain

spectra well below saturation while keeping best signal-to-noise ratio, and they were kept the same throughout the measurements.

First-Principles Calculations

First-principles calculations are implemented under the framework of density functional theory using the Vienna's ab initio simulation package (version 6.3.4). We employ the generalized gradient approximation (GGA) with the parameterization of Perdew-Burke-Ernzerhof optimized for solids^{49,50}. The valence electrons of C (2s²2p²) and H (1s¹) are decided by the projected augmented wave potentials. The cut-off kinetic energy for the plane-wave basis set is 700 eV, which is found sufficient to converge the force acting on each atom to less than 0.01 eV/Å. The unit cells of C₄₈H₂₀ (96 C and 40 H) are used to calculate the electronic structures and their Brillouin zone is sampled by a Monkhorst mesh with 0.2 Å⁻¹ as the spacing between k points. We approximate the long-range pair interactions using the simple D2 method of Grimme⁵¹, with a cut-off radius of 50 Å. At each target pressure, the unit cell is optimized for atomic position, cell shape and cell volume. After structural optimization, we performed a self-consistency cycle using the Heyd-Scuseria-Ernzerhof screened hybrid function (screening factor 0.15)⁵² to obtain the electronic structures, as shown in Fig. 5.

Vibrational Spectroscopy

The high-pressure Raman measurements were performed with a custom-built, highly focused Raman system using a 532 nm laser source. A single-crystal of C₄₈H₂₀ was loaded along with a ruby sphere into the sample chamber of a symmetric Mao-type DAC with 400 μm culet-sized low

fluorescence anvils. Si oil was used as PTM. The measurements were imaged on a CCD, with a typical exposure time of 0.01 s at 0.5 mW laser power. High-pressure mid-IR spectra were recorded using the Bruker VERTEX 70 v IR spectrometer with HYPERION 2000 microscope in transmission mode in the range of 600–5000 cm^{-1} at 2 cm^{-1} per step. The spectrum of an empty DAC at ambient pressure was used as background signal for all measurements. The sample chamber was filled with dicoronylene single crystals and compressed without PTM.

Synchrotron Powder X-Ray Diffraction (SP-XRD) Measurements

High pressure SP-XRD measurements were performed at BL12B2 at SPring-8 (Japan; $\lambda = 0.6199 \text{ \AA}$, beam diameter of 50 μm). Polycrystalline $\text{C}_{48}\text{H}_{20}$ was loaded along with a ruby sphere into the sample chamber of a symmetric Mao-type DAC with 400 μm and 200 μm culet-sized anvils. The sample chamber was completely filled with the sample. Daphne oil was used as PTM and each pressure point was determined by the fitting pressure shift of the ruby fluorescence line. Twenty 60-second scans were acquired and summed to ensure a good signal-to-noise ratio while avoiding the possibility of radiation damage to the sample. The two-dimensional images were integrated with IPAnalyzer and data analysis was performed using the Le Bail pattern decomposition technique within the GSAS-II program suite⁵³.

Synchrotron Single-Crystal X-Ray Diffraction (SC-XRD) Measurements

A single crystal of $\text{C}_{48}\text{H}_{20}$ was screened in-house to check diffraction quality prior to loading. A well-diffracting crystal of approximate dimensions $42 \times 15 \times 10 \mu\text{m}^3$ (LxWxH) was loaded with 2000 bars of He gas as the pressure transmitting medium in a BX90 DAC using diamond anvils with 250 μm culets and a Re gasket. A small (diameter $\approx 3 \mu\text{m}$) grain of gold, and a ruby sphere (diameter $\approx 5 \mu\text{m}$) were included for pressure determination. Collections of SC-XRD data were performed at the pressure post gas loading (3.3 GPa), as well as at 10.4, 19.2, and 26.2 GPa, stopping once the sample was no longer diffracting sufficiently for crystal structure determination.

These SC-XRD experiments were performed at the ID15b beamline of the European Synchrotron Radiation Facility (ESRF) in Grenoble, France. Diffraction experiments used a monochromatic X-ray beam of wavelength 0.4099 \AA and beam spot size of approximately $1.0 \times 1.0 \mu\text{m}^2$, data were collected on a Dectris Eiger2 X CdTe 9 M detector in 0.5° angular steps over a -36 to 36° range. Data were processed using the CrysAlis^{Pro} software⁵⁴ for reflection search, removal of parasitic diamond anvil reflections, unit cell determination, and data integration. Structure solution and model refinement were performed using the Olex2 user interface⁵⁵. Initial structure solution of the first data set (the lowest pressure point) was achieved with intrinsic phasing methods using SHELXT⁵⁶. For the subsequent datasets, the model from the prior pressure point was used as a starting point for least squares refinements of the structure using SHELXL⁵⁷. Hydrogen atoms were constrained to calculated geometries and allowed to ride their parent atoms.

Data availability

All relevant data and single crystal samples are available from the corresponding author. The data that support the findings of this study are available in the Supporting Information. The CCDC number of the dicoronylene, $\text{C}_{48}\text{H}_{20}$, at ambient pressure is 2141267, at 3.3 GPa is 2352043, at 10.4 GPa is 2352046, at 19.2 GPa is 2352045, and at 26.2 GPa is 2352044.

Received: 14 January 2025; Accepted: 23 April 2025;

Published online: 15 May 2025

References

- Wilson, A. H. The theory of electronic semi-conductors. *Proc. Roy. Soc.* **133**, 458 (1931).
- Ashcroft, N. W. Metallic hydrogen: a high-temperature superconductor? *Phys. Rev. Lett.* **21**, 1748–1749 (1968).
- Narayana, C., Luo, H., Orloff, J. & Ruoff, A. L. Solid hydrogen at 342 GPa: no evidence for an alkali metal. *Nature* **393**, 46–49 (1998).
- Loubeyre, P., Occelli, F. & LeToullec, R. Optical studies of solid hydrogen to 320 GPa and evidence for black hydrogen. *Nature* **416**, 613–617 (2002).
- Eremets, M. I. & Troyan, I. A. Conductive dense hydrogen. *Nat. Mater.* **10**, 927–931 (2011).
- Dias, R. P. & Silvera, I. F. Observation of the Wigner-Huntington transition to metallic hydrogen. *Science* **355**, 715–718 (2017).
- Loubeyre, P., Occelli, F. & Dumas, P. Synchrotron infrared spectroscopic evidence of the probable transition to metal hydrogen. *Nature* **577**, 631–635 (2020).
- Ashcroft, N. W. Hydrogen Dominant Metallic Alloys: High Temperature Superconductors? *Phys. Rev. Lett.* **92**, 187002 (2004).
- Eremets, M. I., Trojan, I. A., Medvedev, S. A., Tse, J. S. & Yao, Y. Superconductivity in Hydrogen Dominant Materials: Silane. *Science* **319**, 1506–1509 (2008).
- Drozdov, A. P., Eremets, M. I., Troyan, I. A., Ksenofontov, V. & Shylin, S. I. Conventional superconductivity at 203 kelvin at high pressures in the sulfur hydride system. *Nature* **525**, 73–76 (2015).
- Zhou, D. et al. High-Pressure Synthesis of Magnetic Neodymium Polyhydrides. *J. Am. Chem. Soc.* **142**, 2803–2811 (2020).
- Mitsuhashi, R. et al. Superconductivity in alkali-metal-doped picene. *Nature* **464**, 76–79 (2010).
- Lian, C. S., Wang, J. T., Duan, W. & Chen, C. Phonon-mediated high-Tc superconductivity in hole-doped diamond-like crystalline hydrocarbon. *Sci. Rep.* **7**, 1464 (2017).
- Zhong, G., Yang, C., Chen, X. & Lin, H. Superconductivity in solid benzene molecular crystal. *J. Phys.:Condens. Matter* **30**, 245703 (2018).
- Oehzelt, M. et al. High pressure x-ray study on anthracene. *J. Chem. Phys.* **119**, 1078–1084 (2003).
- Fabbiani, F. P. A., Allan, D. R., Parsons, S. & Pulham, C. R. Exploration of the high-pressure behaviour of polycyclic aromatic hydrocarbons: naphthalene, phenanthrene and pyrene. *Acta Cryst.* **B62**, 826–842 (2006).
- Zhao, X. et al. Structure and Piezochromis of chrysene at high pressures. *Dyes Pigments* **227**, 112161 (2024).
- Zhou, W., Aslandukov, A., Minchenkova, A., Hanfland, M. & Dubrovinsky, L. N. Dubrovinkaia, Structural transformations and stability of benzo[a]pyrene under high pressure. *IUCrJ* **12**, 16–22 (2025).
- Nakagawa, T. et al. Piezochromic luminescence of dicoronylene: Key for revealing hidden Raman modes at high pressure. *Carbon* **197**, 563–569 (2022).
- Zhou W. et al. *Commun Chem.* **7**, 209. <https://doi.org/10.1038/s42004-024-01294-0> (2024)
- Wen, X., Hoffmann, R. & Ashcroft, N. W. Benzene under High Pressure: a Story of Molecular Crystals Transforming to Saturated Networks, with a Possible Intermediate Metallic Phase. *J. Am. Chem. Soc.* **133**, 9023–9035 (2011).
- Zhao, X. M. et al. Combined experimental and computational study of high-pressure behavior of triphenylene. *Sci. Rep.* **6**, 25600 (2016).
- Matsui, A. H. Excitonic processes in aromatic molecular crystals of strong exciton-phonon coupling. *Pure Appl. Chem.* **67**, 429–436 (1995).
- Samara, G. A. & Drickamer, H. G. Effect of Pressure on the Resistance of Fused-Ring Aromatic Compounds. *J. Chem. Phys.* **37**, 474 (1962).
- Shirotani, I., Inokuchi, H. & Minomura, S. Electrical Conduction of Organic Semiconductors under high pressure. *Bull. Chem. Soc. Jpn.* **39**, 386–390 (1966).
- Farina, L. et al. Pentacene at high pressure. *High. Press. Res.* **23**, 349–354 (2003).
- Wang, Q. et al. High pressure electrical transport behavior in organic semiconductor pentacene. *High. Pres. Res.* **34**, 355–364 (2014).
- Hillier, N. J. & Schilling, J. S. Search for metallization in benzene to 209 GPa pressure. *High. Pres. Res.* **34**, 1–8 (2014).

29. Ciabini, L. et al. Triggering dynamics of the high-pressure benzene amorphization. *Nat. Mater.* **6**, 39–43 (2007).
30. Fanetti, S. et al. High-Pressure Optical Properties and Chemical Stability of Picene. *J. Phys. Chem. C*. **117**, 5345–5351 (2013).
31. Rieger, R. & Mullen, K. Polycyclic aromatic hydrocarbons as model cases for structural and optical studies. *J. Phys. Org. Chem.* **23**, 315–325 (2010).
32. Menon, A. et al. Optical band gap of cross-linked, curved, and radical polyaromatic hydrocarbons. *Phys. Chem. Chem. Phys.* **21**, 16240–16251 (2019).
33. Nakagawa, T. et al. Full-color luminescence from single-component hydrocarbon crystal: RGB emission by altering molecular packing under pressure. *Adv. Opt. Mater.* **11**, 2300586 (2023).
34. Song, X. et al. Superconductivity above 105 K in Nonclathrate Ternary Lanthanum Borohydride below Megabar Pressure. *J. Am. Chem. Soc.* **146**, 13797–13804 (2024).
35. Chen, L. C. et al. Synthesis and superconductivity in yttrium-cerium hydrides at high pressures. *Nat. Commun.* **15**, 1809 (2024).
36. Goddard, R., Haenel, M. W., Herndon, W. C., Krüger, C. & Zander, M. Crystallization of large planar polycyclic aromatic hydrocarbons: the molecular and crystal structures of hexabenzob[bc,ef,hi,kl,no,qr] coronene and benzo[1,2,3-bc:4,5,6-b'c']dicononene. *J. Am. Chem. Soc.* **117**, 30–41 (1995).
37. Kubelka, P. & Munk, F. A. Contribution to the Optics of Pigments. *Z. Technol. Phys.* **12**, 593–599 (1931).
38. Makula, P., Pacia, M. & Macyk, W. How to Correctly Determine the band gap energy of Modified Semiconductor photocatalysts based on UV-Vis Spectra. *J. Phys. Chem. Lett.* **9**, 6814–6817 (2018).
39. Costa, J. C. S., Taveira, R. J. S., Lima, C. F. R. A. C., Mendes, A. & Santos, L. M. N. B. F. Optical band gaps of organic semiconductor materials. *Opt. Mater.* **58**, 51–60 (2016).
40. Costa, J. C. S., Campos, R. M., Lima, L. M. S. S., Ribeiro da Silva, M. A. V. & Santos, L. M. N. B. F. On the Aromatic Stabilization of Fused Polycyclic Aromatic Hydrocarbons. *J. Phys. Chem. A* **125**, 3696–3709 (2021).
41. Cai, W., Zhang, R., Yao, Y. & Deemyad, S. Piezochromism and structural and electronic properties of benz[a]anthracene under pressure. *Phys. Chem. Chem. Phys.* **19**, 6216–6223 (2017).
42. van der Pauw, L. J. A method of measuring specific resistivity and Hall effect of discs of arbitrary shape. *Philips Res. Rep.* **13**, 1–9 (1958).
43. Boldyreva, E. V. High-pressure diffraction studies of molecular organic solids. A personal view. *Acta Crystallogr., Sect. A: Found. Crystallogr.* **64**, 218–231 (2008).
44. Shinozaki, A., Kagi, H. & Mimura, K. Formation of amorphous hydrogenated carbon from compression of benzene. *IOP Conf. Ser.: J. Phys.: Conf. Ser.* **950**, 042057 (2017).
45. Fitzgibbons, T. et al. Benzene-derived carbon nanotubes. *Nat. Mater.* **14**, 43–47 (2015).
46. Heibel, G. et al. Chain-length-dependent intermolecular packing in polyphenylenes: a high pressure study. *J. Phys.: Condens. Matter* **15**, 3375–3389 (2003).
47. Oehzelt, M. et al. Crystal structure of oligoacenes under high pressure. *Phys. Rev. B* **74**, 104103 (2006).
48. Angel, R. J., Alvaro, M., Gonzalez-Platas, J. & Alvaro, M. EosFit7c and a Fortran module (library) for equation of state calculations. *Z. Krist.* **229**, 405–419 (2014).
49. Perdew, J. P., Burke, K. & Ernzerhof, M. Generalized gradient approximation made simple. *Phys. Rev. Lett.* **77**, 3865–3868 (1996).
50. Perdew, J. P. Restoring the Density-Gradient Expansion for exchange in solids and surfaces. *Phys. Rev. Lett.* **100**, 136406 (2008).
51. Grimme, S. Semiempirical GGA-type density functional constructed with a long-range dispersion correction. *J. Comput. Chem.* **27**, 1787–1799 (2006).
52. Hummer, K., Harl, J. & Kresse, G. Heyd-Scuseria-Ernzerhof hybrid functional for calculating the lattice dynamics of semiconductors. *Phys. Rev. B* **80**, 115205 (2009).
53. Toby, B. H. & Von Dreele, R. B. GSAS-II: The Genesis of a Modern Open-Source All-Purpose Crystallography Software Package. *J. Appl. Crystallogr.*, **46**, 544–549 (2013).
54. Rigaku Oxford Diffraction, CrysAlisPro Software system, version 1.171.43.67a. (Rigaku Corporation Wroclaw, Poland, 2023)
55. Dolomanov, O. V., Bourhis, L. J., Gildea, R. J., Howard, J. A. K. & Puschmann, H. OLEX2: A complete structure solution, refinement and analysis program. *J. Appl. Cryst.* **42**, 339–341 (2009).
56. Sheldrick, G. M. SHELXT – Integrated space-group and crystal-structure determination. *Acta Cryst.* **A71**, 3–8 (2015).
57. Sheldrick, G. M. Crystal structure refinement with SHELXL. *Acta Cryst.* **C71**, 3–8 (2015).

Acknowledgements

This research was financially supported by the National Key Research and Development program of China (Grant No. 2022YFA1402301 and 2022YFA1405500), the Beijing Natural Science Foundation (Project No. IS24025), and the National Natural Science Foundation of China (Grant No. U2230401, 42150101). D.L. thanks the UKRI Future Leaders Fellowship (MR/V025724/1) for financial support. The SPXRD experiments at BL12B2 at the SPring-8 were performed under SPring-8 proposal No. 2023A4139. The authors acknowledge the European Synchrotron Radiation Facility (ESRF) for the provision of beamtime at the ID15b beamline. For the purpose of open access, the author has applied a Creative Commons Attribution (CC BY) licence to any Author Accepted Manuscript version arising from this submission.

Author contributions

T.N. contributed to conceptualization, funding acquisition, preparing sample, investigations, formal analysis, writing the paper. T.N. K.B. and X.L. performed absorption spectroscopy measurements and analysis. T.N., C.Z. and K.B. performed transport property measurements, T.N. and P.D-S. Performed Raman and IR measurements, T.N., H.L., and N.H. performed high pressure SPXRD. M.V. performed formal analysis of the diffraction data and review&editing the paper. S.B., D.L., A.L., G.G. A.D.R. performed high pressure synchrotron SCXRD and formal analysis of the diffraction data. Q.H. performed all DFT calculations and review&editing the paper. H-k.M. and Y.D. supervised the study, funding acquisition, and review&editing the paper. All authors discussed the results and made substantial input to the writing.

Competing interests

The authors declare no competing interests.

Additional information

Supplementary information The online version contains supplementary material available at <https://doi.org/10.1038/s43246-025-00814-2>.

Correspondence and requests for materials should be addressed to Takeshi Nakagawa or Yang Ding.

Peer review information *Communications Materials* thanks the anonymous reviewers for their contribution to the peer review of this work. Primary Handling Editors: Vishal Govind Rao and Jet-Sing Lee.

Reprints and permissions information is available at <http://www.nature.com/reprints>

Publisher's note Springer Nature remains neutral with regard to jurisdictional claims in published maps and institutional affiliations.

Open Access This article is licensed under a Creative Commons Attribution-NonCommercial-NoDerivatives 4.0 International License, which permits any non-commercial use, sharing, distribution and reproduction in any medium or format, as long as you give appropriate credit to the original author(s) and the source, provide a link to the Creative Commons licence, and indicate if you modified the licensed material. You do not have permission under this licence to share adapted material derived from this article or parts of it. The images or other third party material in this article are included in the article's Creative Commons licence, unless indicated otherwise in a credit line to the material. If material is not included in the article's Creative Commons licence and your intended use is not permitted by statutory regulation or exceeds the permitted use, you will need to obtain permission directly from the copyright holder. To view a copy of this licence, visit <http://creativecommons.org/licenses/by-nc-nd/4.0/>.

© The Author(s) 2025